

Nanoscale

Accepted Manuscript



This is an *Accepted Manuscript*, which has been through the Royal Society of Chemistry peer review process and has been accepted for publication.

Accepted Manuscripts are published online shortly after acceptance, before technical editing, formatting and proof reading. Using this free service, authors can make their results available to the community, in citable form, before we publish the edited article. We will replace this *Accepted Manuscript* with the edited and formatted *Advance Article* as soon as it is available.

You can find more information about *Accepted Manuscripts* in the [Information for Authors](#).

Please note that technical editing may introduce minor changes to the text and/or graphics, which may alter content. The journal's standard [Terms & Conditions](#) and the [Ethical guidelines](#) still apply. In no event shall the Royal Society of Chemistry be held responsible for any errors or omissions in this *Accepted Manuscript* or any consequences arising from the use of any information it contains.

COMMUNICATION

Characterization of Nanoporous Gold Disks for Photothermal Light Harvesting and Light-gated Molecular Release

Cite this: DOI:
10.1039/x0xx00000x

Gregory M. Santos, Fusheng Zhao, Jianbo Zeng, and Wei-Chuan Shih*

Received 00th March 2014,
Accepted 00th March 2014

DOI: 10.1039/x0xx00000x

www.rsc.org/

Nanoporous gold disks (NPGDs) with 400 nm diameter, 75 nm thickness, and 13 nm pores exhibit large specific surface area and effective photothermal light harvesting capability with a conversion efficiency of 56%. A potential application is demonstrated by light-gated, multi-step molecular release of pre-adsorbed R6G fluorescent dye on arrayed NPGDs.

Nanoporous gold (NPG) has attracted intense research interest in recent years due to its large specific surface area, catalytic function, and plasmonic properties.¹⁻⁷ NPG exhibits both propagating surface plasmon resonance (SPR) along the planar metal film surface and localized surface plasmon resonance (LSPR) within its interconnected nanoporous framework. The LSPR-enhanced radiative processes have been the basis of several enhanced optical phenomena, *e.g.*, extinction, surface-enhanced Raman Scattering (SERS), and metal-enhanced fluorescence (MEF).⁸⁻¹¹ On the other hand, LSPR-enhanced non-radiative decay through heat generation provides an alternative light harvesting approach, and has been extensively studied in various gold nanoparticles.¹²⁻¹⁹ The photothermal effect of existing gold nanoparticles (spheres, shells, rods, hollow spheres, etc.) has been well studied and employed for in situ hyperthermia generation and heat-assisted drug delivery,²⁰⁻³³ where detailed photothermal characterization is critical. However, the potential photothermal effect in NPG has not been extensively studied because existing NPG materials are not in the form of nanoparticles.

The determination of the photothermal conversion efficiency (η) has been recently employed as a comparative tool for evaluating photothermal effects of different nanoparticles using energy balance equations.³⁴⁻⁴² Cole *et al.*³⁵ previously reported η values for SiO₂@Au nanoshells, Au₂S@Au nanoshells and Au nanorods using the heat transfer model proposed by Roper *et al.*³⁷ By irradiating the gold nanostructures near the maximum absorption wavelength (815 nm), the conversion efficiencies for Au₂S@Au nanoshells and Au nanorods ($\eta \approx 60\%$) were reportedly higher compared to SiO₂@Au nanoshells ($\eta \approx 30\%$). Certain nanostructural properties that affect the absorption cross section (*i.e.* particle size, geometric shape, resonance

wavelength, surface modifications) contribute to the variation in the calculated η .^{35, 36, 40, 42, 43}

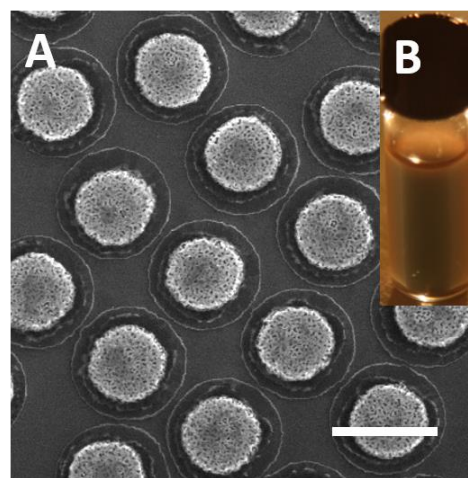


Figure 1. Substrate-bound and colloidal NPGDs: (A) SEM images of NPGDs with 400 nm diameter, 75 nm thickness, and ~13 nm pores. Scale bar is 500 nm; (B) Non-aggregating colloidal NPGDs in aqueous solutions.

Recently, we demonstrated that discrete NPG disks (NPGDs) are excellent plasmonic entities with a SERS enhancement factor exceeding 10^8 (See Figure 1A).⁸ Unlike traditional semi-infinite, planar NPG thin films or bulk NPG ingots, NPGDs of sub-wavelength diameter and sub-100 nm thickness feature LSPR coupling from the internal nanoporous network and the external disk shape. Besides surface-bound array format, NPGDs can also be fabricated as colloidal nanoparticles as shown in Figure 1B, prompting us to investigate their photothermal properties. However, we have decided to perform experiments using surface-bound NPGDs because we can easily quantify their total number, which greatly facilitate experiments. Given the large specific surface area, ease of surface functionalization, and excellent electrical/thermal conductivity,^{2, 6, 24}

44-49 NPGDs has great potential in light harvesting and photothermal applications. However, recent attention has been focused mainly on NPG thin films for catalysis, sensing, and other aspects.^{3-5, 7, 9-11, 47, 50-54}

In this study, we have evaluated the photothermal properties of substrate-bound arrayed NPGDs (Figure 1A) by utilizing thermal imaging to monitor spatially-resolved temperature changes due to light harvesting and heat generation in both water bath and air ambient environment. We show that arrayed NPGD can effectively cause a significant macroscopic temperature rise in the both cases. We also determine the photothermal conversion efficiency for NPGDs. Furthermore, Rhodamine 6G (R6G), a fluorescent dye, is utilized as a model molecule to demonstrate high-capacity, multi-stage, light-gated molecular release from NPGDs.

The fabrication of substrate-bound NPGD arrays involves sputtering an initial film of 120 nm thick Au : Ag (28 : 72) alloy over the glass coverslip (~165 μm thick) by DC sputtering. A monolayer film of 600 nm polystyrene (PS) beads were then deposited on the top surface of the alloy film using a modified Langmuir-Blodgett technique.^{8, 26} Oxygen plasma-etching was then employed to produce isolated beads, then the sample was further etched using Ar plasma-etching to remove the alloy not covered by the isolated beads which allowed for the formation of alloy disks on the glass surface. The alloy disks were then dealloyed using a 70% nitric acid aqueous solution for 1 min followed by rinsing with copious amounts of deionized (DI) water. The dealloying process resulted in disks with a diameter of 400 nm and thickness of 75 nm.⁸ NPGD images (Figure 1 and S2) were obtained using a field emission gun scanning electron microscope (FEI XL-30 FEG SEM, Philips).

To characterize the light harvesting capability of NPGDs, we aimed to quantify the photothermal heat generation where thermal imaging was employed to obtain time-resolved temperature maps. The NPGD arrays were irradiated in water and air media at 1-minute intervals using a tunable continuous wave (CW) near-infrared (NIR) Ti-Sapphire laser (2 mm diameter beam, 0.10 W/mm², 700-900 nm, 3900S, Spectra Physics). Figure S1 in Supplementary Information shows the schematic diagram of the glass chamber used for the water-bath experiments. Thermal maps were acquired from the backside of the glass chamber wall at a slight angle to prevent damage to the infrared camera (A320G, FLIR) recording 16-bit 320x240 pixel images at 60Hz. It has an uncooled focal plane array microbolometer with a spectral range of 7.5 to 13 μm and a temperature sensitivity of 50 millikelvin.

As shown in Figure 2, the NIR laser irradiation was turned on at 15 sec and off at 75 sec. Based on the difference between the ambient temperature and the steady-state temperature (~26 °C), the temperature increase (ΔT) of ~6 °C was measured from the backside of the glass chamber corresponding to the irradiated spot on the NPGD arrays, compared to a barely appreciable temperature increase at the level of room temperature fluctuations for a gold film sample (Figure 2C). The results suggest that the average temperature rise can be achieved under water bath configuration by irradiating the NPGD arrays. Since the temperature measurement was performed on the glass chamber wall, the local temperature on NPGDs would be higher. In addition, the NPGDs appeared to generate prolonged temperature change as evidenced by the higher-than-initial temperature even after the laser irradiation was off. It is interesting to note that a “heat plume”-like pattern appeared in the thermal images for the NPGD sample. This can be explained by convection of the heated water.

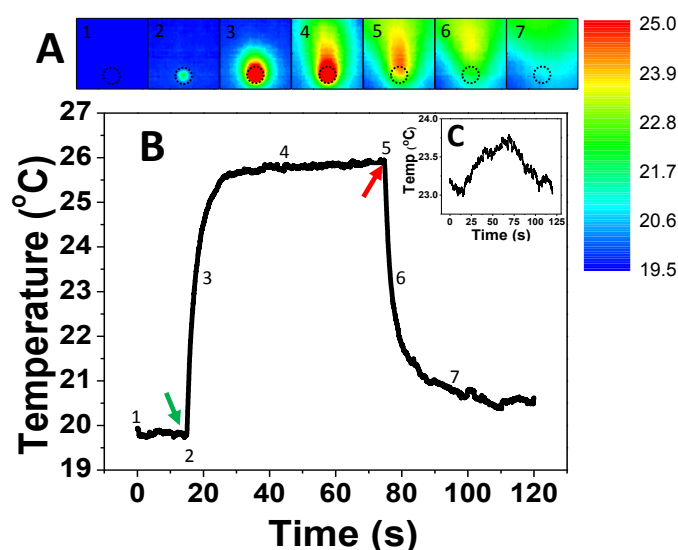


Figure 2. Photothermal heating NPGDs in water: (A) Time-resolved temperature maps and (B) corresponding temperature profile of the irradiated spot (dotted circle, 2 mm in diameter) on the NPGD sample inside a glass chamber filled with water. (C) Temperature profile of irradiated gold film sample. Arrows depicting times when laser was turned on (green) and off (red). Numbers on the profile indicate the corresponding temperature map. Images were recorded from a 10 x 10 mm² area of the backside of the glass chamber wall. Color bar represents temperature in degree Celsius.

The previous experiment showed that the amount of heat generated by water-bathed NPGD arrays can raise the glass chamber wall temperature by ~6 °C. Due to the heat capacity, conductivity, and convection of water, the measured temperature rise can be significantly less than within the immediate location of the nanostructures. Herein, we demonstrate a more “direct” temperature measurement for estimating photothermal conversion efficiency. In this experiment, the NPGD sample was simply held in the air with the laser irradiation incident on the NPGD (“front”) side, and the thermal imaging acquired from the backside. This eliminated any uncertainty and variation in surface emissivity for temperature mapping. The default emissivity was set at 0.95 for the smooth glass surface. As shown in Figure 3A-3C, NPGD samples reached an average temperature rise (ΔT) of ~60 °C within the laser irradiation spot. The temperature profile averaged over the whole sample area is shown in Figure 3C. We note that our experimental configuration appears to be similar to a recently published paper by Guler *et al.* for obtaining thermal imaging data from irradiated arrayed titanium nitride disks in air.⁵⁵

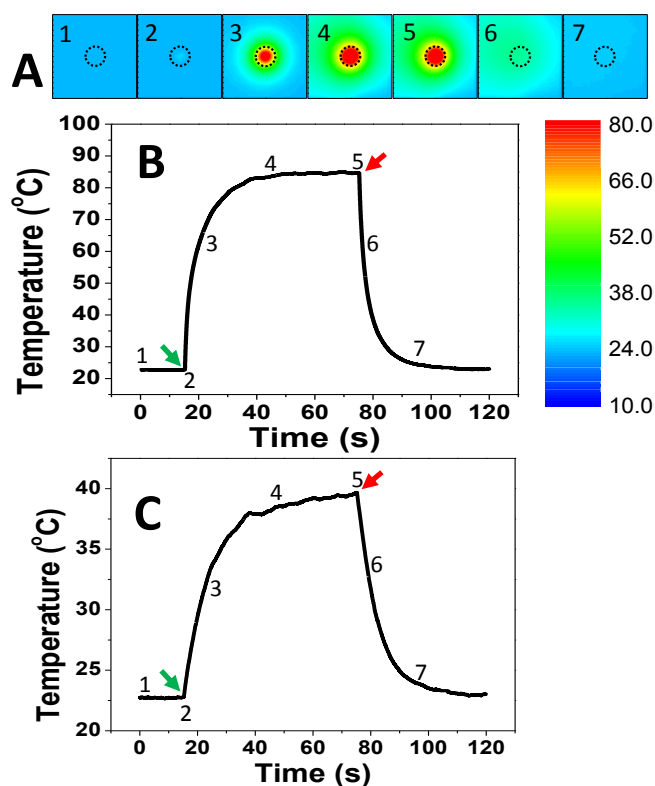


Figure 3. Heating NPGDs in air medium: (A) Time-resolved temperature maps of NPGD arrays in air medium. Each thermal image corresponds to a 10 x 10 mm² area of the backside of the sample. Shared color bar represents temperature in degree Celsius. (B) Temperature profile obtained from the dotted circle indicating the laser irradiation spot in (A). (C) Average temperature profile obtained from the entire sample surface of NPGDs (area: 10 x 10 mm²). Green and red arrows indicate time points when the laser was turned on (green) and off (red), respectively. Numbers on the profile indicate the temperature map sequence.

For reliable determination of photothermal efficiency of NPGDs, the total absorbed laser power, sample size, and gold mass of each sample need to be carefully evaluated. The absorption measurements (Table S2 in Supplementary Information) were calculated from total, reflected and transmitted laser power measurements (PD-300-1W, Ophir). The average buoyant mass of individual NPGDs was ~60 fg as determined by resonant mass measurement (Archimedes, Affinity Biosensors). The number of NPGD particles was manually counted within a representative field of view from optical images of the NPGD samples (Figure S2), and then scaled up to the irradiation spot size or the entire sample area. Total gold mass (listed in Table S1 in the Supplementary Information) was calculated by multiplying the single NPGD mass and the estimated number of disks, and was later incorporated into the calculation of the light-to-heat conversion efficiency. The results for the total absorbed power and total gold mass for the NPGD samples are reported in the Supplementary Information.

In previous studies, a macroscopic heat transfer model was used to determine the photothermal conversion efficiency of gold nanoparticles in solution^{36, 37, 40, 42} and as a solid-state array.³⁸ By following equations proposed by Roper et al.,³⁷ the rate of change in sample temperature is governed by the photothermal heat generation rate due to Au nanoparticles (Q_1) and glass substrate (Q_0), and the heat

dissipation rate to the external environment (Q_{ext}), which can be expressed as

$$\left(\sum_i m_i c_i\right) \frac{dT}{dt} = Q_1 + Q_0 - Q_{ext} \quad (1)$$

where T is the temperature, t is time, m_i is the mass and c_i is the specific heat capacity of component i , respectively. The corresponding values are listed in Table S1. As an example, the calculation for this summation term for NPGD sample was carried out using the following equation

$$\sum_i m_i c_i = m_{Au} c_{Au} + m_{GS} c_{GS} \quad (2)$$

where m_{Au} and m_{GS} are the total mass of gold (NPGD) and glass, respectively, in each sample. c_{Au} and c_{GS} are the corresponding specific heat constants of Au and glass at 25 °C.

The photothermal heat generation rate by the gold materials upon laser exposure can be expressed as

$$Q_1 = (I_o - I_{tr} - I_{refl})\eta = I_{abs}\eta \quad (3)$$

where I_o is the incident laser power (~300 mW). To obtain the absorbed power (I_{abs}), the transmitted and reflected portion (I_{tr} and I_{refl}) of the laser power were determined by additional power measurements as mentioned earlier (see Supplementary Information). The fraction of the laser power converted into heat is the photothermal conversion efficiency (η).

In Eq. (1), the heat dissipated to the external environment is given by

$$Q_{ext} = hA[T(t) - T_{amb}] \quad (4)$$

where h is the heat transfer coefficient (in mW mm⁻² K⁻¹), A is the surface area of the interface between the gold material and the external environment, $T(t)$ is the temperature at time t , and T_{amb} is the ambient room temperature. From Eq. (1), by defining $\Delta T \equiv T(t) - T_{amb}$, the rate of temperature change is expressed as

$$\frac{d\Delta T}{dt} = \frac{I_{abs}\eta + Q_0}{\sum_i m_i c_i} - \frac{hA\Delta T}{\sum_i m_i c_i} \quad (5)$$

The rate constant (B) of heat dissipation to the external environment is defined as:

$$B = \frac{hA}{\sum_i m_i c_i} \quad (6)$$

and can be determined by measuring the source-free decreasing temperature profile from the time when the laser is turned off until the sample returns to the ambient temperature. The temperature trace in this regime can be found by setting $I_{abs}\eta + Q_0 = 0$ in Eq. (5) and solving for $T(t)$ using the limit $T(0) = T_{max}$. Incorporating the B term, the solution to Eq. (5) can be expressed as

$$T(t) = T_{amb} + (T_{max} - T_{amb})e^{-Bt} \quad (7)$$

$$\frac{T(t) - T_{amb}}{T_{max} - T_{amb}} = \theta = e^{-Bt} \quad (8)$$

where T_{max} is the maximum temperature before the laser is turned off. Scaled to steady-state temperature T_{max} . A dimensionless temperature parameter, θ , is introduced as a function of time in Eq. (8). As shown in Figure 4, the rate constant (B) can be obtained as the slope of natural logarithm of θ using the average temporal profile in Figure 3C versus

time. As indicated by the linear behavior of the plot, the temperature drop back to the ambient temperature was shown to behave as a first-order decay process. Since the experimental setup was kept the same for each measurement, the dissipation rate constant was expected to be the same for different irradiation wavelengths, and was observed. At about ~20 sec after the laser was turned off, the temperature starts to plateau back to the ambient temperature, hence, a less linear relationship in Figure 4 is observed. An average heat dissipation rate constant (B) of $\sim 0.14 \text{ s}^{-1}$ is determined for the NPGD samples in the 700-900 nm range.

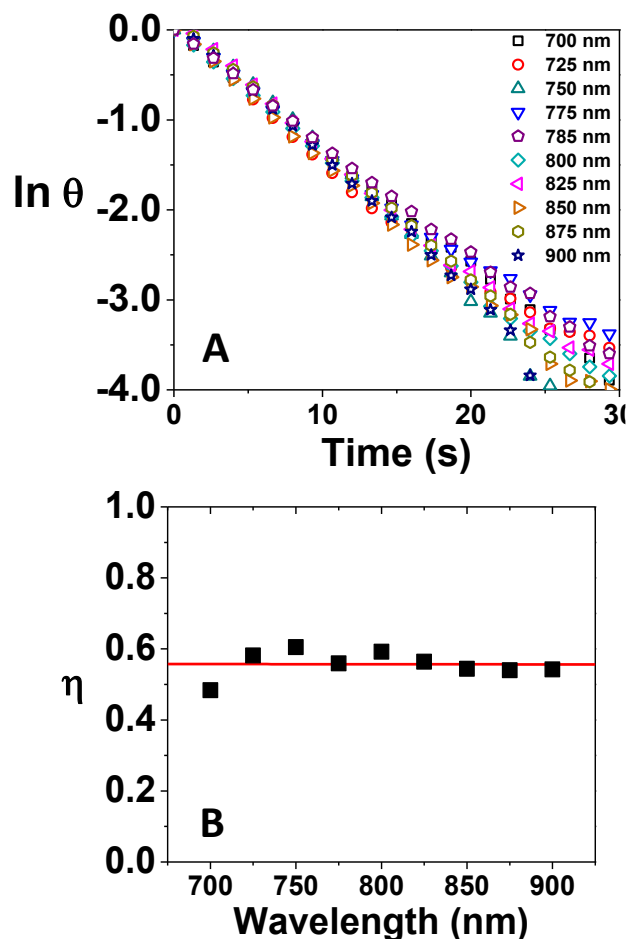


Figure 4. Rate constant and photothermal conversion efficiency for laser irradiation wavelengths ranging from 700-900 nm: (A) Plot of the natural log of θ versus time after the laser was turned off. (B) Photothermal conversion efficiency.

The total amount of heat generated can be directly correlated to the absorbed power (I_{abs}) through the photothermal conversion efficiency. When temperature rise reaches a steady-state as represented by plateau period in temperature profiles in Figure 3, the temperature will remain constant where $Q_1 + Q_0 = Q_{\text{ext}}$ and $\Delta T \equiv T_{\text{max}} - T_{\text{amb}}$. By setting Eq. (5) equal to zero, the average photothermal conversion efficiency of NPGDs was determined to be 56% for the 700-900 nm range. Since the equation for η is normalized to the optical absorption power measurements, η is relatively invariant within the particular range of irradiation wavelengths (see Figure 4B).

From recent photothermal studies, the results for η varies a wide range for other gold nanostructures: spherical nanoparticles (60-80%),

nanoshells (~30%) and nanorods (13-96%).^{35, 36, 42} We note that in these results, the highest efficiency was achieved for small nanoparticles (~10 nm), and the efficiency typically decreases as nanoparticle size increases. Considering the rather large size of NPGD, its efficiency value is in fact surprisingly high compared to the reported nanoparticles that are typically <100 nm. Since NPGD can be viewed as a large cluster of small nanoparticles, and due to the abundant plasmonic surface area within its interconnected ligament system, NPGD is able to maintain a decent photothermal efficiency at a relatively larger size.

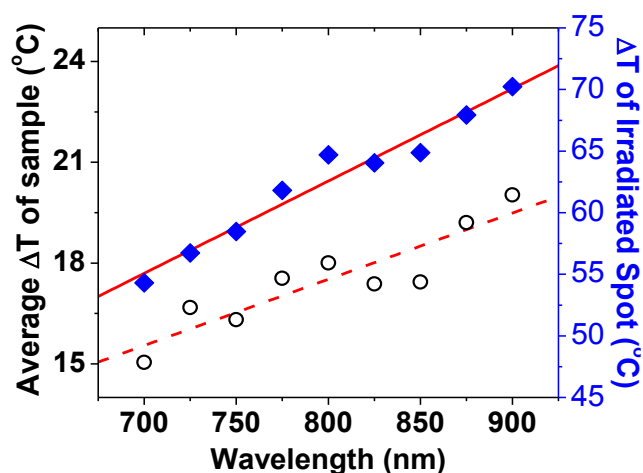


Figure 5. Temperature rise (ΔT) for laser irradiation wavelengths ranging from 700-900 nm: Averaged over the entire sample surface ($10 \times 10 \text{ mm}^2$) in circles and the laser irradiation spot (2 mm in diameter) in diamonds.

Although the photothermal conversion efficiency stays relatively flat for different irradiation wavelengths, the overall heating effect can be quite different. In a recent study by Chen et al.,⁴² the effect of the plasmon wavelength on the photothermal conversion of gold nanostructures was demonstrated where the highest temperature increase occurred when the LSPR wavelength coincided with the irradiation wavelength. By keeping the average input laser power constant (300 mW), the wavelength-dependent heating was indeed observed as shown in Figure 5 where the average ΔT and the local ΔT in the irradiated spot increased with wavelength, which followed a trend similar to that in the extinction spectra (Figure S3) of NPGDs. The gradual increase in ΔT from 700 to 900 nm resulted from the stronger absorption of NPGD towards the longer NIR wavelength region. In Figure S3, the extinction maximum is identified to be at ~1100 nm for NPGDs, far from the irradiation wavelength (700-900 nm). Thus, it is reasonable to expect that a higher temperature can be achieved if irradiation wavelength closer to 1100 nm is employed.

Next, we investigate the potential advantages of NPGD's large specific surface in light-gated molecular delivery. The level of molecular release was quantified by measuring "downstream" laser-induced fluorescence spectrum of R6G fluorescence dye. The fluorescence emission spectra was measured using an optical setup which includes a fiber-coupled spectrometer (CCS200, Thorlabs) and a 532 nm laser excitation source (2 mm diameter beam, 0.5 mW/mm^2 , Millennia V, Spectra Physics). The distance between the heating laser spot and the downstream fluorescence detection laser spot was ~7 mm (center-to-center). The same glass chamber was employed with schematic description shown in Figure S1. As shown in Figure 6, R6G

fluorescence emission spectra (500-700nm) were obtained at various stages of our experiments as discussed below.

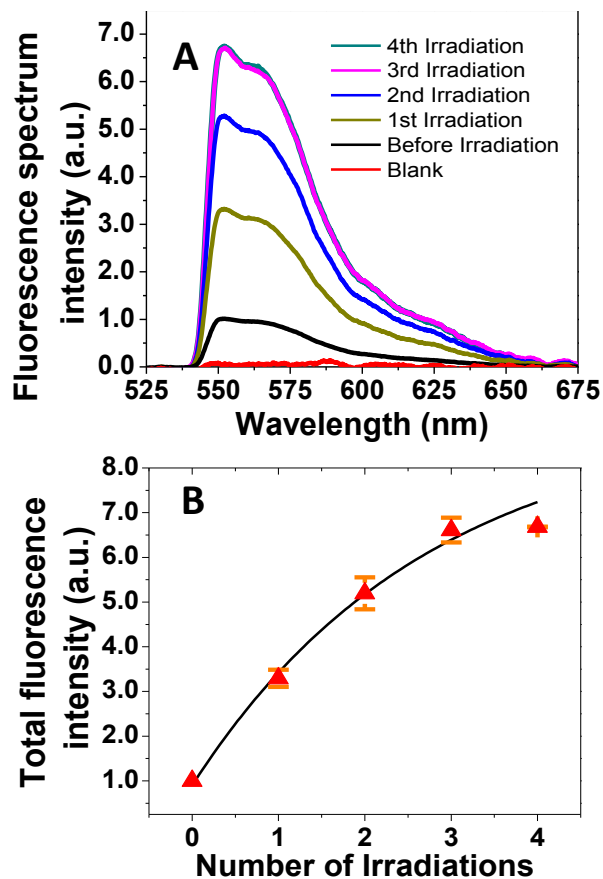


Figure 6. (A) Downstream fluorescence from released R6G molecules: Fluorescence emission spectra of R6G before and after successive laser irradiations of NPGDs arrays. (B) Normalized total intensity of downstream R6G fluorescence.

The NPGD arrays on a glass coverslip were incubated in 100 μM R6G aqueous solutions for 24 hours. Each experiment started with a blank measurement where the glass chamber only contained DI water (700 μL). The R6G-loaded NPGD arrays were then inserted into the glass chamber, and was allowed to equilibrate with the DI water by spontaneously releasing poorly adsorbed or loosely bound R6G molecules, which contributed to the “Before irradiation” fluorescence signals. After the R6G concentration in water ceased changing, as evidenced by no further fluorescence intensity variations, the sample was then irradiated by the same NIR laser with identical power density (2 mm diameter beam, 0.10 W/mm^2) for 5 minutes to induce photothermal desorption of the adsorbed dye molecules.

Concentration equilibrium was achieved after each irradiation before the next irradiation was applied. Fluorescence emission spectra as shown in Figure 6A were acquired at the equilibrium state after each irradiation, and normalized to the “Before irradiation” spectrum in each experiment. Significant increase in fluorescence emission intensity was observed downstream after each irradiation, and started to plateau by the fourth irradiation as shown in Figure 6B. The fluorescence intensity level after four irradiations was ~ 7 times of that before irradiation. The results suggest NPGDs can hold surface adsorbates and permit effective multi-step, light-gated release. This

can be attributed to the larger surface area for molecular adsorption provided by the internal nanoporous network.

The photothermal light-gated release capability of NPGD arrays largely depends on the plasmonic properties. Recent studies^{35, 36, 40} showed that smaller nanoparticle sizes lead to higher efficiency values ($\eta \rightarrow 100\%$) due to lower light scattering contributions to the total extinction coefficient. Surface roughness^{56, 57} of the nanoshells had been shown to alter scattering properties which was known to shift photothermal transduction efficiencies.³⁵ Hence, future NPGD design should include smaller disks and controllable surface morphology (*i.e.* roughness) to optimize absorption-to-extinction ratios. Another important parameter that can be further explored is laser duty cycle. It was demonstrated that mechanically chopping the laser source results in higher photothermal conversion efficiencies³⁷ for gold nanoparticles due to the prevention of temporal hot spots (that result to steam pockets in aqueous medium) that induce localized changes in the absorption of the nanostructures.^{58, 59}

Conclusions

Through the use of time-resolved temperature mapping, the spatial and temporal characteristics of photothermal heating in NPGD arrays is successfully demonstrated for both aqueous and air ambient environments. By applying a thermodynamic model to our experimental data, we determined the photothermal conversion efficiency at 56% for NPGD arrays. As a potential application, light-gated, multi-stage release of pre-adsorbed R6G dye molecules from NPGD arrays has been demonstrated. The results establish the foundation that NPGDs can be employed for photothermal light harvesting and light-gated molecular release.

Acknowledgments

WCS acknowledges funding from the National Science Foundation (NSF) CAREER Award (CBET-1151154), the National Aeronautics and Space Administration (NASA) Early Career Faculty Grant (NNX12AQ44G), the Gulf of Mexico Research Initiative (GoMRI-030) and the Cullen College of Engineering at the University of Houston.

Notes and References

*Department of Electrical and Computer Engineering, University of Houston, 4800 Calhoun Road, Houston, Texas 77204, USA. E-mail: wshih@uh.edu

† Electronic supplementary information (ESI) available: Chemicals and materials used in NPGD fabrication, Thermal Imaging, SEM images and extinction spectra of NPGDs, calculated average mass of materials and power measurements for light absorption at different wavelengths.

1. A. Wittstock, J. Biener, J. Erlebacher and M. Bäumer, *Nanoporous Gold: From an Ancient Technology to a High-Tech Material*, Royal Society of Chemistry, 2012.
2. S. V. Petegem, S. Brandstetter, R. Maass, A. M. Hodge, B. S. El-Dasher, J. r. Biener, B. Schmitt, C. Borca and H. V. Swygenhoven, *Nano Lett.*, 2009, 9, 1158-1163.
3. A. Wittstock, V. Zielasek, J. Biener, C. M. Friend and M. Bäumer, *Science*, 2010, 327, 319-322.
4. T. Fujita, P. Guan, K. McKenna, X. Lang, A. Hirata, L. Zhang, T. Tokunaga, S. Arai, Y. Yamamoto and N. Tanaka, *Nat. Mater.*, 2012, 11, 775-780.
5. Y. Ding and M. Chen, *MRS Bulletin*, 2009, 34, 569-576.

6. F. Yu, S. Ahl, A.-M. Caminade, J.-P. Majoral, W. Knoll and J. Erlebacher, *Anal. Chem.*, 2006, 78, 7346-7350.
7. X. Lang, L. Qian, P. Guan, J. Zi and M. Chen, *Appl. Phys. Lett.*, 2011, 98, 093701-093703.
8. J. Qi, P. Motwani, M. Gheewala, C. Brennan, J. C. Wolfe and W.-C. Shih, *Nanoscale*, 2013, 5, 4105-4109.
9. Y. Fu, J. Zhang, K. Nowaczyk and J. R. Lakowicz, *Chem. Commun. (Cambridge, U. K.)*, 2013, 49, 10874-10876.
10. X. Y. Lang, P. F. Guan, L. Zhang, T. Fujita and M. W. Chen, *Appl. Phys. Lett.*, 2010, 96, -.
11. X. Y. Lang, P. F. Guan, T. Fujita and M. W. Chen, *Phys. Chem. Chem. Phys.*, 2011, 13, 3795-3799.
12. S. Link, C. Burda, M. B. Mohamed, B. Nikoobakht and M. A. El-Sayed, *J. Phys. Chem. A*, 1999, 103, 1165-1170.
13. S. Link, C. Burda, B. Nikoobakht and M. A. El-Sayed, *J. Phys. Chem. B*, 2000, 104, 6152-6163.
14. S. Link, A. Furube, M. B. Mohamed, T. Asahi, H. Masuhara and M. A. El-Sayed, *J. Phys. Chem. B*, 2002, 106, 945-955.
15. G. Baffou, P. Berto, E. Bermúdez Ureña, R. Quidant, S. Monneret, J. Polleux and H. Rigneault, *ACS Nano*, 2013, 7, 6478-6488.
16. G. Baffou, P. Bon, J. Savatier, J. Polleux, M. Zhu, M. Merlin, H. Rigneault and S. Monneret, *ACS Nano*, 2012, 6, 2452-2458.
17. G. Baffou, R. Quidant and F. J. García de Abajo, *ACS Nano*, 2010, 4, 709-716.
18. J. S. Donner, G. Baffou, D. McCloskey and R. Quidant, *ACS Nano*, 2011, 5, 5457-5462.
19. G. Baffou and H. Rigneault, *Phys. Rev. B*, 2011, 84, 035415.
20. W. Lu, C. Xiong, G. Zhang, Q. Huang, R. Zhang, J. Z. Zhang and C. Li, *Clin. Cancer Res.*, 2009, 15, 876-886.
21. X. Huang, I. H. El-Sayed, W. Qian and M. A. El-Sayed, *Nano Lett.*, 2007, 7, 1591-1597.
22. S. Lal, S. E. Clare and N. J. Halas, *Acc. Chem. Res.*, 2008, 41, 1842-1851.
23. M.-R. Choi, K. J. Stanton-Maxey, J. K. Stanley, C. S. Levin, R. Bardhan, D. Akin, S. Badve, J. Sturgis, J. P. Robinson, R. Bashir, N. J. Halas and S. E. Clare, *Nano Lett.*, 2007, 7, 3759-3765.
24. E. Detsi, S. Punzhin, J. Rao, P. R. Onck and J. T. M. De Hosson, *ACS Nano*, 2012, 6, 3734-3744.
25. R. Laocharoensuk, S. Sattayasamitsathit, J. Burdick, P. Kanatharana, P. Thavarungkul and J. Wang, *ACS Nano*, 2007, 1, 403-408.
26. J. Z. Zhang, *J. Phys. Chem. Lett.*, 2010, 1, 686-695.
27. A. M. Gobin, M. H. Lee, N. J. Halas, W. D. James, R. A. Drezek and J. L. West, *Nano Lett.*, 2007, 7, 1929-1934.
28. J. Young, E. Figueroa and R. Drezek, *Ann Biomed Eng.*, 2012, 40, 438-459.
29. E. Day, P. Thompson, L. Zhang, N. Lewinski, N. Ahmed, R. Drezek, S. Blaney and J. West, *J Neurooncol*, 2011, 104, 55-63.
30. C. Loo, A. Lowery, N. Halas, J. West and R. Drezek, *Nano Lett.*, 2005, 5, 709-711.
31. X. Wu, T. Ming, X. Wang, P. Wang, J. Wang and J. Chen, *ACS Nano*, 2009, 4, 113-120.
32. M. P. Melancon, W. Lu, Z. Yang, R. Zhang, Z. Cheng, A. M. Elliot, J. Stafford, T. Olson, J. Z. Zhang and C. Li, *Mol. Cancer Ther.*, 2008, 7, 1730-1739.
33. C. Fang, L. Shao, Y. Zhao, J. Wang and H. Wu, *Adv. Mater. (Weinheim, Ger.)*, 2012, 24, 94-98.
34. Q. Tian, F. Jiang, R. Zou, Q. Liu, Z. Chen, M. Zhu, S. Yang, J. Wang, J. Wang and J. Hu, *ACS Nano*, 2011, 5, 9761-9771.
35. J. R. Cole, N. A. Mirin, M. W. Knight, G. P. Goodrich and N. J. Halas, *J. Phys. Chem. C*, 2009, 113, 12090-12094.
36. K. Jiang, D. A. Smith and A. Pinchuk, *J. Phys. Chem. C*, 2013, 117, 27073-27080.
37. D. K. Roper, W. Ahn and M. Hoepfner, *J. Phys. Chem. C*, 2007, 111, 3636-3641.
38. A. G. Russell, M. D. McKnight, A. C. Sharp, J. A. Hestekin and D. K. Roper, *J. Phys. Chem. C*, 2010, 114, 10132-10139.
39. V. P. Pattani and J. W. Tunnell, *Lasers in Surgery and Medicine*, 2012, 44, 675-684.
40. H. H. Richardson, M. T. Carlson, P. J. Tandler, P. Hernandez and A. O. Govorov, *Nano Lett.*, 2009, 9, 1139-1146.
41. J. Hu, B. Li, Q. Wang, R. Zou, x. liu, K. Xu and W. Li, *Nanoscale*, 2014, DOI: 10.1039/C3NR06242B.
42. H. Chen, L. Shao, T. Ming, Z. Sun, C. Zhao, B. Yang and J. Wang, *Small*, 2010, 6, 2272-2280.
43. R. Jiang, S. Cheng, L. Shao, Q. Ruan and J. Wang, *J. Phys. Chem. C*, 2013, 117, 8909-8915.
44. E. Seker, Y. Berdichevsky, K. J. Staley and M. L. Yarmush, *Adv. Healthc. Mater.*, 2012, 1, 172-176.
45. J. Biener, G. W. Nyce, A. M. Hodge, M. M. Biener, A. V. Hamza and S. A. Maier, *Adv. Mater. (Weinheim, Ger.)*, 2008, 20, 1211-1217.
46. D. Wang and P. Schaaf, *J. Mater. Chem.*, 2012, 22, 5344-5348.
47. A. Wittstock, B. Neumann, A. Schaefer, K. Dumbuya, C. Kubel, M. M. Biener, V. Zielasek, H.-P. Steinruck, J. M. Gottfried, J. Biener, A. Hamza and M. Baumer, *J. Phys. Chem. C*, 2009, 113, 5593-5600.
48. Y. Sun and T. J. Balk, *Metall and Mat Trans A*, 2008, 39, 2656-2665.
49. X. Lang and M. Chen, *Nanoporous Gold: From an Ancient Technology to a High-Tech Material*, Edited by Arne Wittstock etc, Royal Society of Chemistry; 2012.
50. V. Zielasek, B. Jürgens, C. Schulz, J. Biener, M. M. Biener, A. V. Hamza and M. Bäumer, *Angew. Chem. Int. Ed. Engl.*, 2006, 45, 8241-8244.
51. S. O. Kucheyev, J. R. Hayes, J. Biener, T. Huser, C. E. Talley and A. V. Hamza, *Appl. Phys. Lett.*, 2006, 89, 053102-053102-053103.
52. L. Zhang, L. Chen, H. Liu, Y. Hou, A. Hirata, T. Fujita and M. Chen, *J. Phys. Chem. C*, 2011, 115, 19583-19587.
53. M. M. Biener, J. Biener, A. Wichmann, A. Wittstock, T. F. Baumann, M. Baumer and A. V. Hamza, *Nano Lett.*, 2011, 11, 3085-3090.
54. J. Snyder, T. Fujita, M. Chen and J. Erlebacher, *Nat. Mater.*, 2010, 9, 904-907.
55. U. Guler, J. C. Ndukaife, G. V. Naik, A. G. A. Nnanna, A. V. Kildishev, V. M. Shalaev and A. Boltasseva, *Nano Lett.*, 2013, 13, 6078-6083.
56. C. Oubre and P. Nordlander, *J. Phys. Chem. B*, 2005, 109, 10042-10051.
57. H. Wang, G. P. Goodrich, F. Tam, C. Oubre, P. Nordlander and N. J. Halas, *J. Phys. Chem. B*, 2005, 109, 11083-11087.
58. E. Lukianova-Hleb, Y. Hu, L. Latterini, L. Tarpani, S. Lee, R. A. Drezek, J. H. Hafner and D. O. Lapotko, *ACS Nano*, 2010, 4, 2109-2123.
59. E. Y. Hleb, Y. Hu, R. A. Drezek, J. H. Hafner and D. O. Lapotko, *Nanomedicine*, 2008, 3, 797-812.